Ab initio Simulation of Spin-Charge Qubits based on Bilayer Graphene-WSe_2 Quantum Dots

Author(s):
Ge, Huaiyu; Koopmann, Peter; Mrcarica, Filip; Schmidt, Otto T. P.; Bouquet, Ilan; Dossena, Mauro; Luisier, Mathieu; Cao, Jiang

Publication date:
2025

Permanent link:
https://doi.org/https://doi.org/10.3929/ethz-b-000738574

Originally published in:
npj 2D Materials and Applications 9(1), https://doi.org/10.1038/s41699-025-00568-y

Funding acknowledgement:
- NCCR MARVEL Agility Plus Projekt ()
- NCCR SPIN ()

npj | 2D materials and applications

Article

Published in partnership with FCT NOVA with the support of E-MRS

https://doi.org/10.1038/s41699-025-00568-y

Ab initio simulation of spin-charge qubits based on bilayer graphene-WSe_2 quantum dots

Huaiyu Ge [1,2], Peter Koopmann [1,2], Filip Mrcarica [1,2], Otto T. P. Schmidt [1,2], Ilan Bouquet [1], Mauro Dossena [1], Mathieu Luisier [1] ✉ & Jiang Cao [1] ✉

We propose a spin-charge qubit based on a bilayer graphene and WSe_2 van der Waals heterostructure that together form a quantum dot and demonstrate its functionality from first-principles simulations. Electron and hole confinement as well as electrically controllable spin-orbit coupling (SOC) are modeled by self-consistently solving the Schrödinger and Poisson equations with material parameters extracted from density functional theory as inputs. In both electron and hole quantum dots, we find a two orders of magnitude enhancement of SOC (1.8 meV) compared to intrinsic graphene, in the layer directly adjacent to WSe_2. Time-dependent investigations of the quantum device reveal rapid qubit gate operation in the order of picoseconds. Our simulations indicate that bilayer graphene and WSe_2 heterostructures provide a promising platform for the processing of quantum information.

A variety of different qubit platforms are currently being investigated to identify which materials, engineering processes, and underlying physical mechanisms can be scaled up to large-scale quantum computing units. The most promising architectures are those providing fault-tolerant computing, i. e., overcoming a quantum error threshold for a given quantum code. In this category, the superconducting qubits have shown record gate fidelity as well as fast gate operating times in the order of tens of nanoseconds[1]. However, superconducting systems face scalability challenges due to the heavy circuitry they require. Besides that, they are highly sensitive to environmental noise and material defects, which results in fluctuating relaxation and dephasing times in the microseconds range[2–4]. The second mature platform for fault-tolerant quantum computing takes advantage of the silicon complementary metal-oxide-semiconductor (Si-CMOS) technology and its high scalability potential[5,6]. Using isotopically enriched Si in Si/SiGe heterostructures, quantum gates displaying below-threshold fidelity have been achieved for electron spin qubits[7,8]. Nevertheless, encoding the information into the spin state of the electron requires the adjunction of a macro-magnet to artificially enhance the spin interaction, which complicates the structure design. In the last few years, introduction of germanium as hosting material, in combination with hole quantum dot (QD) architectures has helped circumvent the aforementioned limitation by leveraging the stronger intrinsic spin-orbit interaction found in the valence band of this material[9–11].

Bilayer graphene (BLG) has been identified as another promising material to realize spin qubits[12–15] since it exhibits notably longer spin relaxation times than silicon, up to 50 miliseconds[16]. Applying a vertical electric field on BLG can open an appreciable band gap, which is absent in single-layer graphene. It further allows for electrostatic confinement of charged carriers[17]. Electrostatically-defined BLG QDs with precise control of the number of charged carriers have been demonstrated[18]. However, they are characterized by low spin-orbit coupling (SOC), which makes the effective reading and manipulation of the spin state challenging. A possible approach to significantly enhance SOC in BLG consists of stacking it with a transition metal dichalcogenide (TMDC) layer such as WSe_2 or MoS_2[14,19]. These TMDCs possess a strong SOC due to the extended *d* orbitals of their heavy-metal atoms. Through the proximity effect[19], the SOC of the adjacent graphene layer increases from about 24 μeV in the pristine case to a few meV when placed in contact with a TMDC[19,20]. The boosted SOC in the graphene layer adjacent to the TMDC enables efficient manipulations of spin states via *ac* electric fields and the resulting electric dipole spin resonance (EDSR)[21,22].

The control and measurement of electronic charges are more straightforward compared to spin states. In a semiconductor double quantum dot (DQD) coupled through inter-dot tunneling, the position of a single electron isolated in the left or right QD can be used to encode the qubit information. Coherent manipulation of DQD charge qubits has been observed in silicon and GaAs[23–26], together with correlated two-qubit interactions[27]. Non-invasive state readout has been achieved using a quantum point contact charge detector placed next to the DQD[26]. However, charge noise also strongly couples to these qubits, giving rise to rapid dephasing, except for the special operation point called “sweet spot”. The latter is located near the anti-crossing point where the two qubit eigenstates are delocalized. Hence, it is less sensitive to the potential fluctuation of the QDs. The Landau-Zener-Stückelberg Interference (LZSI) scheme[28] has been

[1]Integrated Systems Laboratory, ETH Zurich, Zurich, Switzerland. [2]These authors contributed equally: Huaiyu Ge, Peter Koopmann, Filip Mrcarica, Otto T. P. Schmidt. ✉e-mail: mluisier@iis.ee.ethz.ch; jiacao@iis.ee.ethz.ch

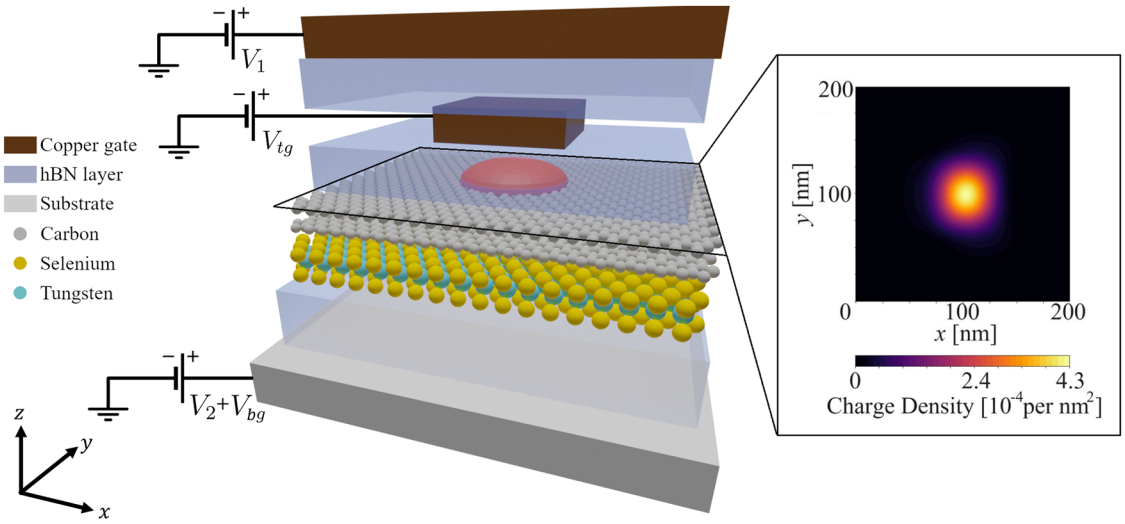

Fig. 1 | Schematic view of the proposed BLG-WSe_2 QD device. The structure measures 200 nm × 200 nm in the *xy*-plane with two top gates in brown and a bottom gate (substrate) in grey. A potential V_1 is applied to the upper top gate electrode, a smaller potential V_{tg} to the lower one, which acts as a confinement gate and is of size 80 nm × 80 nm. Another potential $V_2 + V_{bg}$ is applied to the substrate. V_1 and V_2 generate a vertical electric field E through the BLG-WSe_2 heterostructure. The latter is encapsulated between two hexagonal boron nitride (hBN) dielectric layers (in semi-transparent blue), and placed between the top gates and the substrate. A quantum dot, depicted in red, is confined in the BLG. The inset shows the electron charge distribution in the *xy*-plane at a top gate voltage V_{tg} = 4.91 mV and E = 0.25 V/nm.

proposed to operate charge qubits at their sweet spot and to implement universal single-qubit gate operating at the picosecond scale, with high fidelity[23,29].

It is an attractive option to harness the long coherence time of spin qubit and the ease of charge qubit manipulation. The possibility to encode quantum information in various states within specific degrees of freedom (DoF) of a given physical system has been previously demonstrated[30–32]. Simultaneous entanglement within multiple DoF, known as hyper-entanglement[33], offers a viable route towards vastly increased numbers of entangled qubits. Early experiments could already demonstrate the existence for example of hyper-entangled photon states[31,34]. In this work, we propose a BLG-based device that can entangle the spin and charge DoF of an electrostatically confined charged carrier. It is illustrated in Fig. 1: The BLG-WSe_2 vdW heterostructure (vdWh), encapsulated by dielectrics, is stacked between top and bottom gate electrodes that confine the charge density. The gate-controllable layer polarization of BLG[17] allows the charge qubit to exploit this DoF in the van der Waals (vdW) material and to encode quantum information with it. In contrast to ordinary DQD setups, vdW-based charge qubits reside in a single QD controlled by an electric field vertically applied to the 2D material, thus leading to a more compact footprint and tighter overlap with control gates. As a result, we show that picosecond rotations of the proposed vdW charge qubits can be achieved using the LZSI scheme. On top of that, the enhanced and gate-tunable SOC in the graphene layer adjacent to WSe_2 induces an EDSR that can be harnessed to electrically drive the electron spin through the gate electrodes and a static in-plane magnetic field. By leveraging both mechanisms (EDSR and LZSI), the spin and charge DoF of the device in Fig. 1 can both be manipulated and efficiently entangled.

While graphene-WSe_2 heterostructures have been studied in recent works[19,35,36], the SOC strength and energy levels in electrically confined QDs have not yet been determined. The precise characterization of these quantities is therefore a goal of utmost importance to assess the potential of such qubits and to optimize their performance. To do so, all required material parameters are obtained from ab initio calculations using density functional theory (DFT). The latter method returns the electronic structure of the BLG-WSe_2 vdWh. Subsequently, we confine electron and hole QDs in BLG via the gate electrodes and extract relevant QD properties, including effective dot area, shape, and energy levels. This is realized by performing self-consistent Schrödinger-Poisson simulations. Finally, based on the calculated QD properties, we demonstrate that the proposed BLG-WSe_2 device can potentially sustain fast operations and entanglement on the spin and charge DoF of charged carriers.

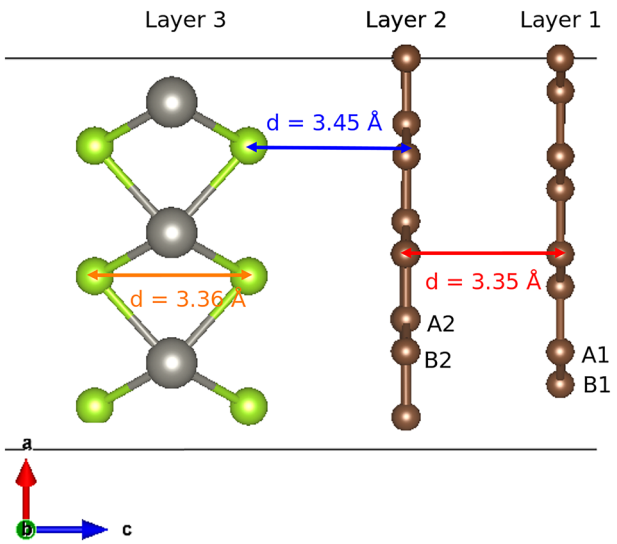

Fig. 2 | Side view and schematic picture of the modeled heterostructure. The super-cell consists of 4 × 4 bilayer graphene unit-cells and 3 × 3 WSe_2 unit-cells. The C, W, Se atoms are represented by brown, gray, and green spheres, respectively. Each bilayer graphene unit-cell consists of A, B nonequivalent C atoms in layer 1 (non-adjacent to WSe_2) and layer 2 (adjacent to WSe_2).

Results

Ab initio band structure and SOC

All DFT simulations are carried out with the Vienna Ab initio Simulation Package (VASP)[37]. We start with unit cell lattice constants a_0^{BLG} = 2.4689 Å for BLG and $a_0^{WSe_2}$=3.2919 Å for WSe_2. Then, we construct an optimized commensurate super-cell with 4 × 4 BLG and 3 × 3 WSe_2 unit cells, as shown in Fig. 2, which leads to less than 0.8% lattice mismatch in both materials and is consistent with the literature values[38]. The observed difference comes from the fact that both unit cells must be slightly strained to stack them on top of

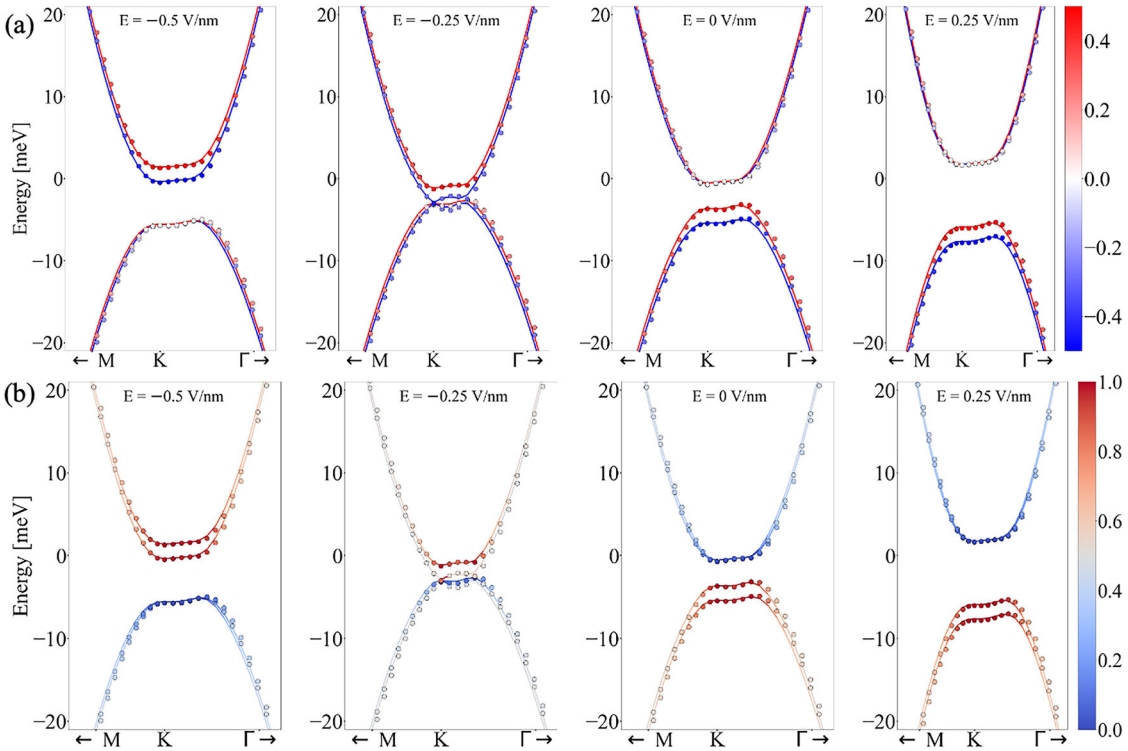

Fig. 3 | Band structure of BLG-WSe_2 vdWh around the *K* point in the Brillouin zone. From left to right, band structure for different transverse electric field magnitudes from −0.5 V/nm to 0.25 V/nm. The DFT results from VASP (symbols) are fitted with an 8-band k · p model (solid lines) in the vicinity of the *K* point. **a** The colors represent the spin projection: spin up (red), spin down (blue). **b** The colors represent the layer projection: adjacent layer 2 (red), non-adjacent layer 1 (blue).

each other while keeping the dimensions of the resulting super-cell small. Then, the entire heterostructure is relaxed until the residual forces acting on each ion are below 10^{-4} eV/Å and the total energy difference between two subsequent self-consistent field iterations is smaller than 10^{-6} eV. More details about our ab initio simulations are given in **Methods**.

The electronic band structure of the BLG-WSe_2 vdWh is then computed along the $M \rightarrow K \rightarrow \Gamma$ path of its Brillouin zone. Results for different transverse electric fields E applied perpendicularly to the BLG-WSe_2 interface are reported in Fig. 3. We first consider the case without any electric field ($E = 0$): A clear band gap is observed in the electronic structure. It originates from the spontaneous polarization of the two graphene layers due to the heterostructure. As a consequence, an electric dipole pointing from WSe_2 towards BLG is generated, which in turn leads to a built-in electric field[19] breaking space inversion symmetry and opening up a band gap of 2.87 meV. The energy of the states predominantly coming from the BLG layer adjacent (non-adjacent) to WSe_2 is lowered (increased) and forms the valence (conduction) band of the vdWh, as shown by the layer projection in the bottom row of Fig. 3.

In pristine BLG, the intrinsic SOC is very small because the valence electrons mostly sit in the p_z orbitals, which have vanishing angular momentum. In the BLG-WSe_2 vdWh, SOC is enhanced since the BLG orbitals hybridize with the WSe_2 ones and the latter exhibit a strong SOC[20]. Since wave functions exponentially decay in space, this hybridization is more prominent for the orbitals of the graphene layer situated closer to WSe_2, thus enhancing its SOC, compared to its more distant counterpart. Therefore, only states originating from the graphene layer adjacent to WSe_2 split due to SOC, whereas those coming from the second graphene layer remain approximately degenerate. This phenomenon is known as *proximity effect*. As the states coming from the adjacent graphene layer constitute the valence band of the vdWh, only these states are split due to SOC for $E = 0$, as confirmed in Fig. 3. Our band structure calculations display the expected layer-selective spin splitting, as previously observed by Gmitra et al.[19].

By applying an external electric field $|E| > 0$, band splitting can be tuned to either the valence or conduction band. A positive electric field amplifies the built-in electric field, therefore keeping the splitting in the valence band, and increasing the band gap to even larger values. Conversely, a negative electric field counters the built-in electric field and brings the conduction and valence bands closer together. When the external electric field completely cancels the built-in electric field, the band gap closes. This condition corresponds to the anti-crossing point of the charge qubit, since the wavefunctions of the conduction band minimum (CBM) and valence band maximum (VBM) delocalize in both graphene layer. For strongly negative electric fields, the band gap increases and the layer projection of the bands are reversed. The conduction band is mostly formed by the atomic orbitals adjacent to WSe_2: splitting between spins is then observed in the conduction band, as shown in Fig. 3. Hence, the external electric field E acts as a knob to modulate the SOC enhancement and move it either to the CBM or VBM. In a BLG-WSe_2 heterostructure, the SOC in the adjacent graphene layer can be increased up to 1.78 meV, which is approximately 100 times its intrinsic value (24μeV).

To study the operation principle of the BLG-WSe_2 qubit system a model as accurate as DFT, but computationally less intensive, is highly desirable. From the projected density-of-states of this system, it appears that the eight conduction and valence bands near its Fermi level, the energy range of interest, originate from the BLG only, while the bands from WSe_2 are located at much higher energies. The influence from WSe_2 can therefore be treated as a small perturbation to the BLG Hamiltonian, which can be accurately represented by an 8-band k · p model. The entries of this Hamiltonian can be adjusted by fitting the eight DFT bands located near the Fermi level of the BLG-WSe_2 vdWh around its K-point, as originally suggested by Konschuh et al. to model BLG[38]

$$\mathcal{H} = \mathcal{H}_{\text{orb}} \otimes s_0 + \mathcal{H}_{\text{soc}} + E_D. \quad (1)$$

This Hamiltonian comprises an orbital part $\mathcal{H}_{\rm orb}$, a spin-orbit coupling part $\mathcal{H}_{\rm soc}$ as well as a global energy shift E_D. The spin-orbit term, $\mathcal{H}_{\rm soc}$, captures the intrinsic and the proximity SOC. The influence of WSe_2 on BLG is intrinsically accounted for in DFT and is therefore captured by the k · p model through the SOC parameters. For each BLG layer j the combined spin-orbit Hamiltonian is given by

$$\mathcal{H}^{j}_{\rm soc} = \begin{pmatrix} \tau\lambda_I^{A_j} s_z & \mathrm{i}(\lambda_0 + 2\lambda_R)s_-^{\tau} \\ -\mathrm{i}(\lambda_0 + 2\lambda_R)s_+^{\tau} & -\tau\lambda_I^{B_j} s_z \end{pmatrix}, \quad (2)$$

where λ_0 refers to the intrinsic SOC, $\lambda_I^{A_j}$ and $\lambda_I^{B_j}$ to the Ising-type SOC of layer j susceptible to the proximity effect. Additionally, λ_R denotes the Rashba coupling arising from the breaking of space-inversion symmetry and from the applied electric field, $\tau = \pm 1$ distinguishes the K, K'-point, whereas the s_i represent the spin operators defined in **Methods**. The value of these fitting parameters can be found in Table 1.

We note that $\pm V$ in this model describes the potential between the upper and lower graphene layers. As expected, V changes almost linearly with E. It has a finite value at $E = 0$ because of the spontaneous polarization of the heterostructure. The Ising-type SOC parameters $\lambda_I^{A_1}$ and $\lambda_I^{A_2}$ of the non-adjacent and adjacent graphene layers are very different due to the presence of WSe_2 and its proximity effect, which is found to be insensitive to the electric field E. The Rashba and intrinsic SOC parameters (λ_R and λ_0) are larger for $E > 0$. We would like to highlight that the band structures obtained from the k · p model and from the DFT calculations agree well over a wide range of energies, as demonstrated in Fig. 3.

Table 1 | Fitting parameters of the chosen 8-band k · p model for the BLG − WSe_2 vdWh

E	V	Δ	$\lambda_I^{A_1}$	$\lambda_I^{A_2}$	λ_0	λ_R	E_D
−0.5	−3.041	6.957	0	1.77	−0.206	0.455	−2.535
−0.25	−0.483	6.783	0	1.743	−0.144	0.501	−2.523
0	1.977	6.751	0	1.777	0.052	0.195	−2.54
0.25	4.259	6.642	0	1.752	−0.162	0.449	−2.522

The electric field is given in units of V/nm, the remaining parameters in meV. The coupling parameters in $\mathcal{H}_{\rm orb}$ (see **k·p model**) are field-independent and equal to $\gamma_0 = 2.558$eV, $\gamma_1 = 0.332$eV, $\gamma_3 = 0.226$eV, and $\gamma_4 = -0.139$eV.

Formation of an electrostatically induced quantum dot

Gate-induced single quantum dot confinement is studied by self-consistently solving the Schrödinger and Poisson equations (details of the solver are given in **k·p model**), based on the aforementioned 8-band k · p Hamiltonian fitted to the DFT bands at finite electric field E. The uniform electric field E is generated by the upper top gate with potential V_1 and the bottom gate with potential V_2, as shown in Fig. 1. The influence of E on the k · p Hamiltonian is accounted for through the potential V (see Table 1). A positive V amplifies the built-in field of BLG-WSe_2 heterostructure, while a negative one counters it and reverses the layer polarization. Hereafter, we use symmetric values of $\pm V$, namely ±4.259 meV, to emulate opposite layer polarization. The corresponding parameters from Table 1 enter our k · p model as they allow for the strongest confining potential. These values of V correspond to electric fields E = 0.25 V/nm ($+V$) and $E \simeq -0.75$ V/nm ($-V$).

The lower top gate with potential $V_{\rm tg}$ controls the local potential distribution underneath and laterally confines the electron or hole quantum dots. The $V_{\rm tg}$-induced electrostatic potential is calculated via the Poisson equation and includes the charge density obtained from the Schrödinger equation. It is then added to the main diagonal elements of the discretized k · p Hamiltonian matrix in real space. The details of our method and simulations are provided in **Methods**.

From the single-dot device shown in Fig. 1, we can extract the dot area and QD energy levels at different top and bottom gate voltages $V_{\rm tg}$ and $V_{\rm bg}$ based on the self-consistent solution of Schrödinger-Poisson calculations. The $V_{\rm tg}$ and $V_{\rm bg}$ values used to create an electron ($V_{\rm tg} > 0$, $V_{\rm bg} < 0$) or hole ($V_{\rm tg} < 0$, $V_{\rm bg} > 0$) dot are the same for the $+V$ and $-V$ cases.

First, our simulations demonstrate electrostatically induced quantum dots in BLG-WSe_2 and reveal the dependence of the dot area and shape on the confining voltages. By varying the top gate voltage $V_{\rm tg}$, we can better

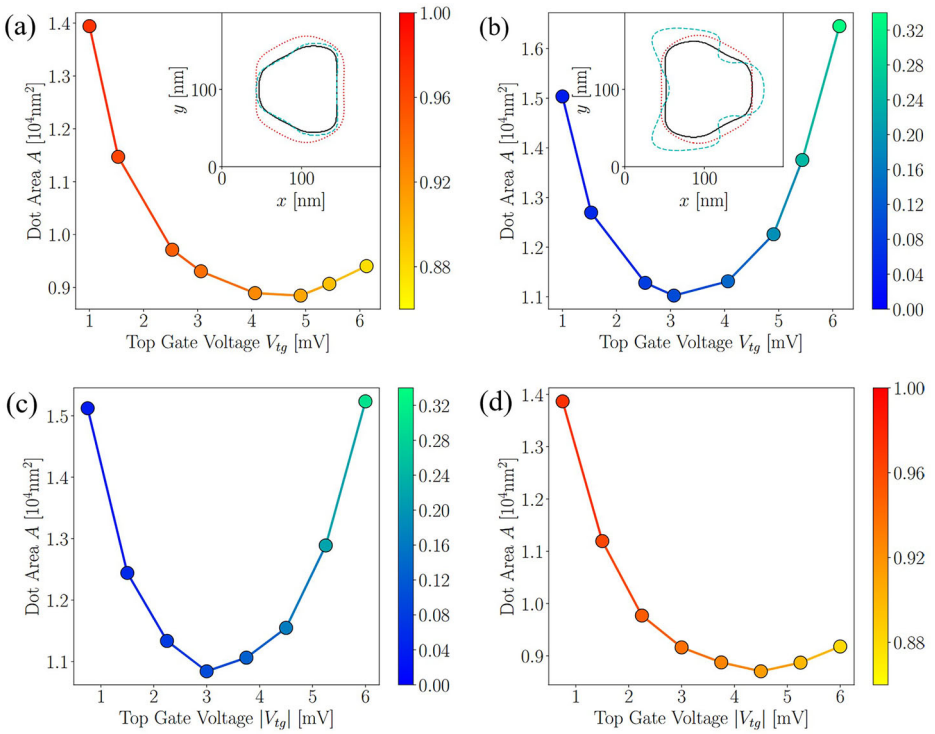

Fig. 4 | Dot area and charge contour lines at different confining potential. Dot area (vertical axis) versus $V_{\rm tg}$ gate voltage (horizontal axis) for **a** electron dot at $+V$, **b** electron dot at $-V$, **c** hole dot at $+V$, and **d** hole dot at $-V$. The colors of the symbols and lines refer to the projected weight of the ground-state to the top graphene layer in BLG. A value of 1 (0) indicates that the dot is fully encompassed in the top (bottom) graphene layer. Layer mixing occurs at large $|V_{\rm tg}|$. The insets in **a** and **b** represent the charge contour lines at the minimum $V_{\rm tg}$ (red dotted), maximum $V_{\rm tg}$ (cyan dashed), and for the minimum dot area (black solid).

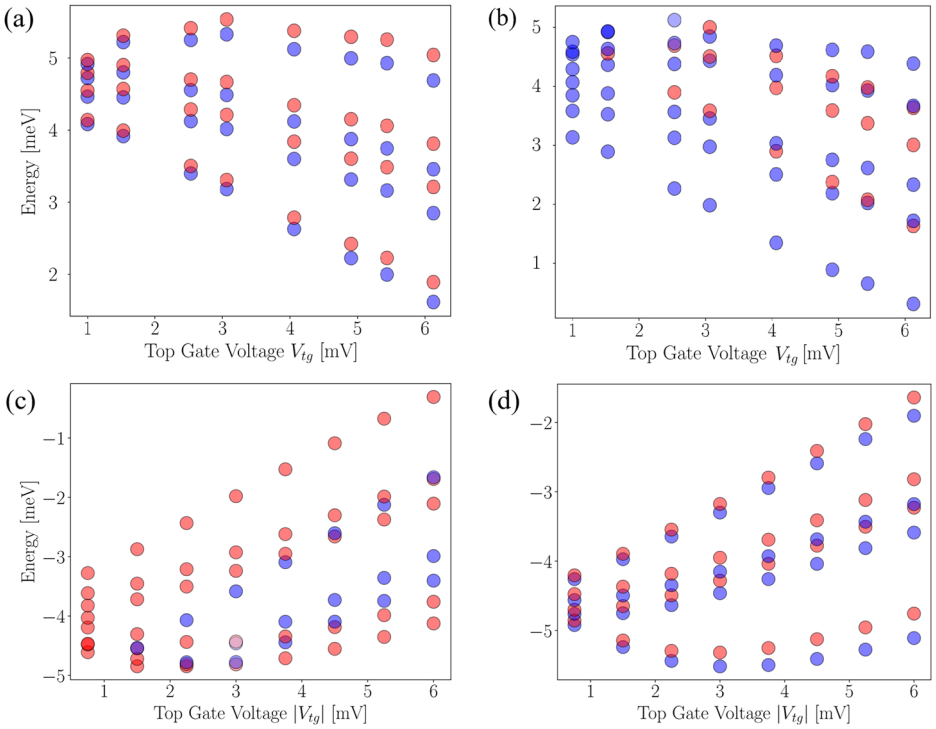

Fig. 5 | Energy levels of electron and hole dots at different confining potential. The lowest electron energy levels of an electron dot in the BLG-WSe_2 system of Fig. 1 are shown for the **a** $+V$ and **b** $-V$ cases as a function of V_{tg}. Sub-plots **c** and **d** show the highest hole energy levels of a hole dot formed in the same system as before, for the $+V$, and $-V$ cases, respectively. The horizontal axis is the applied top gate voltage in mV, and the vertical axis is the energy in meV. The red and blue points correspond to spin-up and spin-down states, respectively.

Table 2 | Energy splitting ΔE_{soc} between the first spin-down and spin-up states versus top gate voltage V_{tg} for electron and hole dots in the $\pm V$ cases, at an applied electric field E = 0.25 V/nm

Elec.	**V_{tg} (mV)**	**1.53**	**2.53**	**3.06**	**4.06**	**4.91**	**5.44**	**6.13**
ΔE_{soc} (meV)	$+V$	0.08	0.10	0.13	0.16	0.20	0.23	0.28
	$-V$	1.67	1.63	1.60	1.55	1.49	1.42	1.32
Hole	**V_{tg} (mV)**	**−1.50**	**−2.25**	**−3.00**	**−3.75**	**−4.50**	**−5.25**	**−6.00**
ΔE_{soc} (meV)	$+V$	1.67	1.64	1.60	1.56	1.52	1.45	1.35
	$-V$	0.08	0.10	0.12	0.15	0.18	0.22	0.26

confine charge density, as reported in Fig. 4 for the electron and hole QDs in the $+V$ and $-V$ cases. The dot area is defined as the isosurface encompassing 95% of the charge density of the first eigenstate above (i.e., electron QD) or below (i.e., hole QD) the Fermi level. In all four cases, as $|V_{tg}|$ increases, the dot area decreases at first, but re-increases after reaching a minimum value. To shed light on this trend and the variation of the dot shape, the contour lines of the charge densities corresponding to the minimum and maximum V_{tg} and the minimum dot area are plotted as insets in Fig. 4a and b. At larger $|V_{tg}|$, the dot changes from nearly a circular to a curved triangular shape, while still keeping the three-fold symmetry of the crystal structure. Further increase of $|V_{tg}|$ leads to an even more distorted dot shape.

Second, we find that increasing $|V_{tg}|$ also induces stronger layer mixing in BLG. The projection of the first electron eigenstate to the top graphene layer is encoded in the color of the lines in Fig. 4. In the $+V$ ($-V$) case of an electron dot, the first eigenstate has contribution mostly from the top (bottom) layer of BLG, as shown in Fig. 4a and b. Increasing V_{tg} from 1 mV to approximately 5 mV (close to the bandgap value of 7 meV) decreases the contribution from the dominant layer from 100% to around 88%, indicating enhanced layer mixing. The layer mixing results in a charge density extending into the graphene layer with larger electrical potential energy. This distorts the dot shape and increases the dot area, explaining the optimum V_{tg} with minimum dot area. Overall, a less uniform dot shape has been linked to enhanced device performance[39]. The curvature in the dot shape has been shown to potentially increase the Rabi oscillation of the spin qubit in germanium planar quantum dots[39]. Therefore, the performance of the qubit can be optimized by tuning V_{tg} through which the dot shape can be modified. A similar effect is also observed for hole dots for which a negative V_{tg} is used, as in Fig. 4c and d.

Next, we turn to the energy spectrum and study the splitting between the first spin-up and spin-down eigenstates near the Fermi level, which define the two energy levels of a spin qubit. Figure 5 presents the calculated electron and hole energy levels for the $+V$ and $-V$ cases. The electrostatic potential to confine hole dots is obtained by reversing the polarity of V_{tg} and V_{bg} and solving self-consistently the Schrödinger and Poisson equations. As shown in Fig. 5a and b, and summarized in Table 2, in the electron system, a larger energy splitting between the first spin-down and spin-up states, ΔE_{soc}, is found for the $-V$ case than for $+V$, up to 1.67 meV, indicating that SOC is enhanced with $-V$. In contrast, in the hole system depicted in Fig. 5c and d, the situation is reversed since the charge is located in the opposite layer, compared to the electron system. The enhancement of SOC is observed for the $+V$ case. Overall, the SOC is larger when the resulting QD is mostly located in the graphene layer adjacent to WSe_2. We also observe that the ΔE_{soc} of the electron dot in the $+V$ case, and of the hole dot in the $-V$ case, slightly increases with V_{tg}. This phenomenon is caused by an increase in layer mixing at higher V_{tg}, as can be seen in Fig. 4.

When SOC is enhanced, as shown in Fig. 5b and c, the energy splitting between the spin-up and spin-down states becomes comparable with the energy difference between the ground- and first-excited spin-down states, allowing unwanted transitions from the spin qubit state to the excited orbital state to happen. This highlights the necessity to further increase the confinement and excited-state energy. However, for electron/hole dots, a

decrease/increase in the energy of the confined states is observed as $|V_{tg}|$ increases, due to the strengthening of the confining potential. The energy of the unconfined hole/electron states below/above the bandgap remains mostly unchanged (not shown here). This behavior leads to a decrease in the QD bandgap as the confinement potential increases. Since maintaining a sizable bandgap is important to achieve carrier confinement, in practice, one needs to simultaneously control $|V_{tg}|$ and the vertical electric field through the potential difference $(V_1 - V_2)$, which gives rise to well-confined carriers with strong SOC.

Finally, we remark that a symmetry relationship emerges between the electron and hole energy level spectrum of the BLG-WSe_2 system. It results from the time-reversal and particle-hole symmetries. The electron dot in the $\pm V$ case is symmetric with the hole dot in the $\mp V$ case, with opposite spin polarization. Such symmetry highlights the possibility of manipulating both electron and hole spin qubits in BLG-WSe_2 vdWh with a similar device setup. This unique feature makes the proposed system an attractive testbed to study arrays of electron and hole spin qubits placed next to each other inside a single chip.

Gate operation for the spin-charge qubit

The BLG-WSe_2 vdWh provides two physical DoF that can be leveraged for quantum information processing. First, charged carriers confined in the QD possess an intrinsic spin that allows one to define a spin qubit. Second, these carriers are formed by the superposition of orbital states that originate from the top and bottom graphene layer, denoted hereafter as $|\mathrm{T}\rangle$ and $|\mathrm{B}\rangle$, respectively, giving rise to a vdW charge qubit[40,41]. Through both DoF, we create a two-qubit system within a single QD. As the nature of the spin and charge (or layer) DoF is different, so are their control mechanisms. These two mechanisms can be described by specific Hamiltonians. Both of them are derived below for the BLG-WSe_2 heterostructure. We then use a Trotter decomposition to simulate the unitary time evolution of the system of interest. These simulations provide a first estimate for the single-qubit gate operation speed and the combined manipulations of both qubits.

Manipulations of the spin qubit via EDSR. The spin qubit can be controlled by *Electric Dipole Spin Resonance* (EDSR) via a time-dependent *perpendicular* (through the vdWh) electric field $\boldsymbol{E}(t) = (E_0 + \tilde{E}\cos(\omega_{ac}t))\boldsymbol{e}_z$ with frequency ω_{ac} generated by the gate electrodes. To avoid changes of the electrons orbital wavefunction, the inter-layer bias should not exceed the anti-crossing point so that the bandgap does not close. The anti-crossing point is reached for $|\boldsymbol{E}| \simeq -0.16$V nm. Therefore, we choose $E_0 \geq 0$Vnm and $E_0 \leq -0.5$V nm and $\tilde{E} \ll |E_0|$. We apply a static *in-plane* magnetic field, without loss of generality along the x-direction $\boldsymbol{B} = B_0\boldsymbol{e}_x$, to define two Zeeman basis states $\{|\leftarrow\rangle, |\rightarrow\rangle\}$. Because of the *ac* electric field, the SOC experienced by the confined charged carrier becomes time-dependent and acts as an oscillating magnetic field that induces transitions between the Zeeman states. Through this EDSR mechanism, when the frequency of the time-dependent SOC matches the Zeeman energy, spin rotation occurs, and the spin states can be electrically driven. The spin dynamics of the BLG-WSe_2 structure during EDSR can be traced through a quantitative and time-dependent model. For this, we consider the two different sources of SOC in the BLG-WSe_2 vdWh.

First, the linear Rashba SOC couples the spin to the oscillation of charge carriers in the transverse direction due to the applied *ac* electric field[21]. The resulting time-dependent Rashba spin interaction Hamiltonian for one graphene layer reads

$$H_{\mathrm{R}} = H_Z + \frac{1}{2}\boldsymbol{h}(t)\cdot\boldsymbol{s}, \tag{3}$$

with the Zeeman term $H_Z = \frac{1}{2}g\mu_B B_0 s_x$,

$$\boldsymbol{h}(t) = 2g\mu_B\boldsymbol{B}\times\boldsymbol{\Omega}(t), \tag{4}$$

and

$$\boldsymbol{\Omega}(t) = \frac{-e}{m_e^*\omega_0^2}l_{\mathrm{R}}^{-1}\begin{bmatrix}0\\0\\\tilde{E}\cos(\omega_{ac}t)\end{bmatrix}. \tag{5}$$

Here, ω_0 is the frequency of the harmonic confinement of the QD, m_e^* the effective electron mass, and $\boldsymbol{s} = (s_x, s_y, s_z)$ a vector of Pauli matrices on the spin. The confinement strength can be extracted from Fig. 5 by taking the energy difference between the ground and first-excited energy levels of the same spin, i.e., for $-V$ we have $\hbar\omega_0 \simeq 1$ meV. Furthermore, we introduce the spin-orbit length l_R due to Rashba SOC. This parameter is related to the extracted Rashba coefficient λ_R via $l_R = (v_F\hbar)/\lambda_R$, which follows by comparing the low-energy Dirac Hamiltonian in Eq. (11) with the linear momentum Rashba Hamiltonian given in ref. 21. The Fermi velocity v_F can be estimated from the intra-layer hopping parameter $\gamma_0 = 2.55$ eV (Table 1) and the BLG lattice constant $a = 2.46$ Å. This gives a value $v_F = (\sqrt{3}a\gamma_0)/(2\hbar) \simeq 8.25\times10^5$ ms^{-1}[42]. With $\lambda_R \simeq 0.5$ meV (Table 1) we have $l_R \simeq 1.08\,\mu$m. Transforming H_R into the rotating frame of the time-dependent electric field, we obtain the interaction spin Hamiltonian for Rashba SOC

$$H_{\mathrm{R}} = g\mu_B B_0\frac{e\tilde{E}}{m_e^*\omega_0^2}l_R^{-1}s_y. \tag{6}$$

The second contribution is the Ising SOC, which is field-independent but layer-selective. Due to the proximity effect, the graphene layer adjacent to WSe_2 has a much stronger Ising SOC. The *ac* field, therefore, modulates the total Ising SOC by varying the layer polarization of BLG. Depending on the static working point E_0 and the *ac* amplitude $\tilde{E}$, the total Ising SOC oscillates over time with a tunable amplitude. In the BLG-WSe_2 vdWh, the layer polarization of the conduction or valence band as a function of the applied field $E(t)$ can be fitted to a sigmoid function based on our self-consistent Schrödinger-Poisson results, as plotted in Fig. 6 (a). By extracting

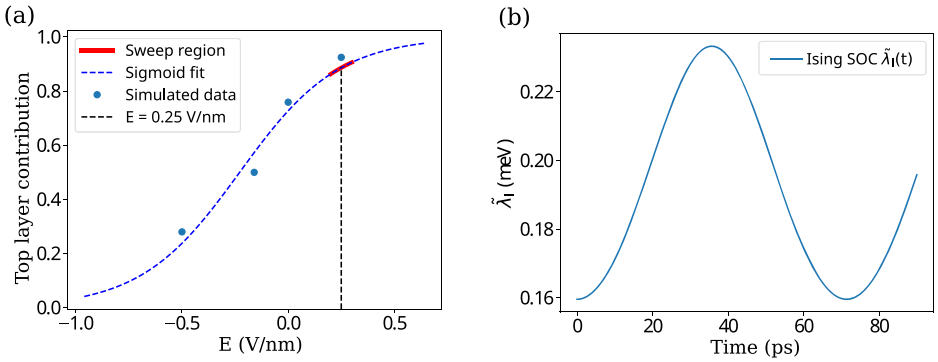

Fig. 6 | Time-dependence of the Ising SOC. a Top layer contribution of the conduction band for different E field values. The sweeping region around $E_0 = 0.25$ Vnm^{-1} (marked by the black dashed line) for $\tilde{E} = 0.05$ Vnm^{-1} is plotted in red segment, the simulated data is denoted by the points, with the Sigmoid fit shown by the blue dashed line. **b** Resulting time-dependent Ising SOC in meV as a function of time, again for $E_0 = 0.25$ V nm^{-1} and $\tilde{E} = 0.05$ V nm^{-1} and with $\omega_{ac} = \epsilon_Z/\hbar = 0.088$ GHz.

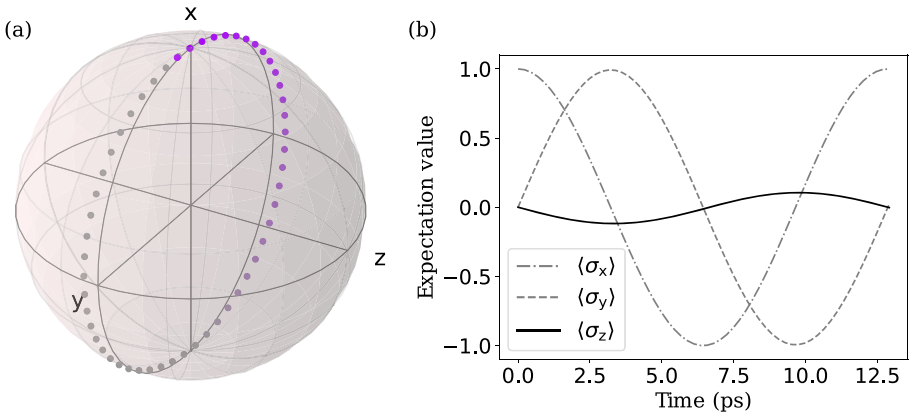

Fig. 7 | State evolution of the spin qubit. a State trajectory for the spin state on a Bloch sphere for an EDSR pulse. The color of the dots indicates the time evolution, i.e., early times in gray and later times in purple. Since Rashba- and Ising-type SOC act on the *y*- and *z*-axis of spin, respectively, both rotations can be seen on the sphere. In this setup, the Ising rotations dominate the Rashba ones. **b** Corresponding expectation values for the σ_x (grey dot dashed line), σ_y (grey dashed), and σ_z (black solid line) spin operators.

the layer polarization at different electric field strengths from the fitted sigmoid function, we can compute the time-dependent contribution of the total Ising SOC, referred to as $\tilde{\lambda}_I(t, E_0, \tilde{E})$, and define the interaction spin Hamiltonian for Ising SOC

$$H_I = \tilde{\lambda}_I(t, E_0, \tilde{E}) s_z. \tag{7}$$

The evolution of the total Ising SOC over time is displayed in Fig. 6b for $E_0 = 0.25$ V nm^{-1} and $\tilde{E} = 0.05$ Vnm^{-1} and with $\omega_{ac} = \epsilon_Z/\hbar = 0.088$ GHz.

The complete EDSR Hamiltonian incorporates contributions from both the Rashba SOC and the Ising SOC. The total spin Hamiltonian under the rotating wave approximation is given by

$$H_{EDSR}(t, E_0, \tilde{E}) = \underbrace{g\mu_B B_0 \frac{e\tilde{E}}{m_e^* \omega_0^2} l_R^{-1} s_y}_{\text{Rashba}} + \underbrace{\tilde{\lambda}_I(t, E_0, \tilde{E}) s_z}_{\text{Ising}}, \tag{8}$$

where s_y and s_z are the Pauli matrices acting on the spin DoF. The contribution of the Ising SOC is incorporated through $\tilde{\lambda}_I$. Using reasonable experimental parameters $E_0 = 0.25\,\text{Vnm}^{-1}$, $\tilde{E} = 0.05\,\text{Vnm}^{-1}$, $B_0 = 0.5$ mT, and the electron effective mass of BLG ($m_e^* = 0.03\, m_0$[43]), we can estimate the constant prefactor C_R of the Rashba term in H_{EDSR} as $C_R := g\mu_B B_0 \frac{e\tilde{E}}{m_e^* \omega_0^2} \approx 18.8$ meV nm. The *ac* electric field frequency, ω_{ac}, is tuned to match the Zeeman energy splitting $\epsilon_Z = g\mu_B B_0 = 0.058$ μeV. The frequency spectrum of the *ac* field lies well below the quantization energy of the harmonic confinement $\hbar\omega_0 \simeq 1$ meV. This prevents orbital excitation of the charge carriers via the EDSR *ac* drive. With $l_R \simeq 1.08$ µm, we find that $C_R l_R^{-1} \approx 17.4$ µeV, which is the energy of spin rotations due to Rashba SOC.

Note that for the EDSR operation, the two sources of SOC, Rashba and Ising, are controlled very differently: The Rashba SOC is layer-independent and sensitive to magnetic fields, whereas the Ising contribution is layer-dependent and insensitive to magnetic fields. This fact can be exploited to tune the desired balance of both SOC contributions. Also, note that the spin rotation axis differs for both mechanisms: The Rashba SOC rotates around the *y*-axis because the *ac*- and *B*-field have been chosen along the spatial *z*- and *x*-direction, respectively. However, the Ising SOC acts as a rotation along the *z*-axis of spin. This is due to the form of the low-energy Dirac Hamiltonian in Eq. (2).

Using the TROTTERQRTE package of the QISKIT modeling framework[44], we simulate the dynamics of the spin qubit with the ab initio calibrated parameters from above. Based on our simulations, we obtain the state trajectory of the spin qubit during an EDSR pulse, as shown in Fig. 7a. We observe that since the Ising SOC is much stronger than the Rashba SOC in our case, the spin trajectory is mostly rotating within the *xy* plane. In addition, we plot in Fig. 7b the expectation values for the spin operators and estimate the speed of a *Z* gate, $R_z(\theta = \pi)$ (rotation around the *z*-axis by π radians), to be $t_{\text{spin}} \simeq 7$ps. This value is obtained for $E_0 = 0.25$ Vnm^{-1} and $\tilde{E} = 0.05$ Vnm^{-1}.

Manipulations of the vdW charge qubit via LZSI. In analogy to the Mach-Zehnder interferometry (MZI), we use the *Landau-Zener-Stückelberg Interference* (LZSI)[24] to rotate the charge DoF. This is composed of three successive steps: (I) The energy eigenstates of the charge qubit are non-adiabatically moved to the anti-crossing point from far away and across it, which implements a unitary action U_{LZ} composed of *z*- and *x*-rotations and can be seen as the action of a beam splitter in the MZI analogy. To achieve an *X* gate, we tune the velocity of potential change $v = |dV/dt|$ such that the *x*-rotation corresponds to a $\pi/2$-rotation (see Supplementary Information for derivation). This initial process is referred to as the first *Landau-Zener transition* (LZ) and is represented by the segment $A \to B \to C$ on the Bloch sphere representation in Fig. 8a, where the red lines indicate *x*-rotations, the green lines *z*-rotations; (II) the two energy eigenstates acquire a phase difference φ_p during a specific time t_{LZSI}, which acts as a rotation $R_z(\varphi_p(t_{\text{LZSI}}))$, as represented by the segment $C \to D$ (purple line); (III) the system is moved back again over the anti-crossing point to the initial position far away from it, implementing the second LZ, represented by the segment $D \to E \to F \to G$. Similar as in MZI, this second transition acts as a final beam splitter, leading to destructive or constructive interference of the energy eigenstates depending on the accumulated phase difference.

The LZSI mechanism effectively enables us to implement a rotation gate $R_x(\theta(t_{\text{LZSI}}))$ for the charge qubit states $\{|\text{T}\rangle, |\text{B}\rangle\}$. In addition, due to the presence of the proximity effect and layer-selective Ising SOC in the BLG, fast spin rotation is also observed during the phase accumulation step, which can be seen in the oscillation of $|B\rangle \otimes |\leftarrow\rangle$ and $|B\rangle \otimes |\rightarrow\rangle$ probabilities in the time evolution plot in Fig. 8b. The combined dynamics of spin and charge qubits during this process can be represented by the quantum circuit in Fig. 8c. This is composed of operators U_{LZ} and $R_z(\varphi_p)$ acting on the charge qubit and the controlled rotation CR_z of the spin qubit with charge qubit as control bit. From this controlled action on the spin DoF, it is also evident that the spin- and charge-qubits become entangled during the phase accumulation. As indicated in Fig. 8a, the Bloch vector goes into the *interior* of the sphere, with an oscillating Bloch vector length $|\boldsymbol{r}| = r$ due to entanglement ($C \to D$). The geometry of entangled states of two qubits is difficult to visualize. Here, we simply project the density matrix of the charge qubit onto the Bloch sphere. The mixed states are projected to vectors with $r < 1$, and the state with maximum entanglement is projected to the origin ($r = 0$). We investigate the entanglement between charge and spin qubits separately in the next section.

However, despite the presence of Ising SOC, it is still possible to implement pure charge rotation, because the spin dynamics is governed by the Ising SOC that is independent of the LZSI and constant over time as a material parameter of the BLG-WSe_2 heterostructure. We investigate the

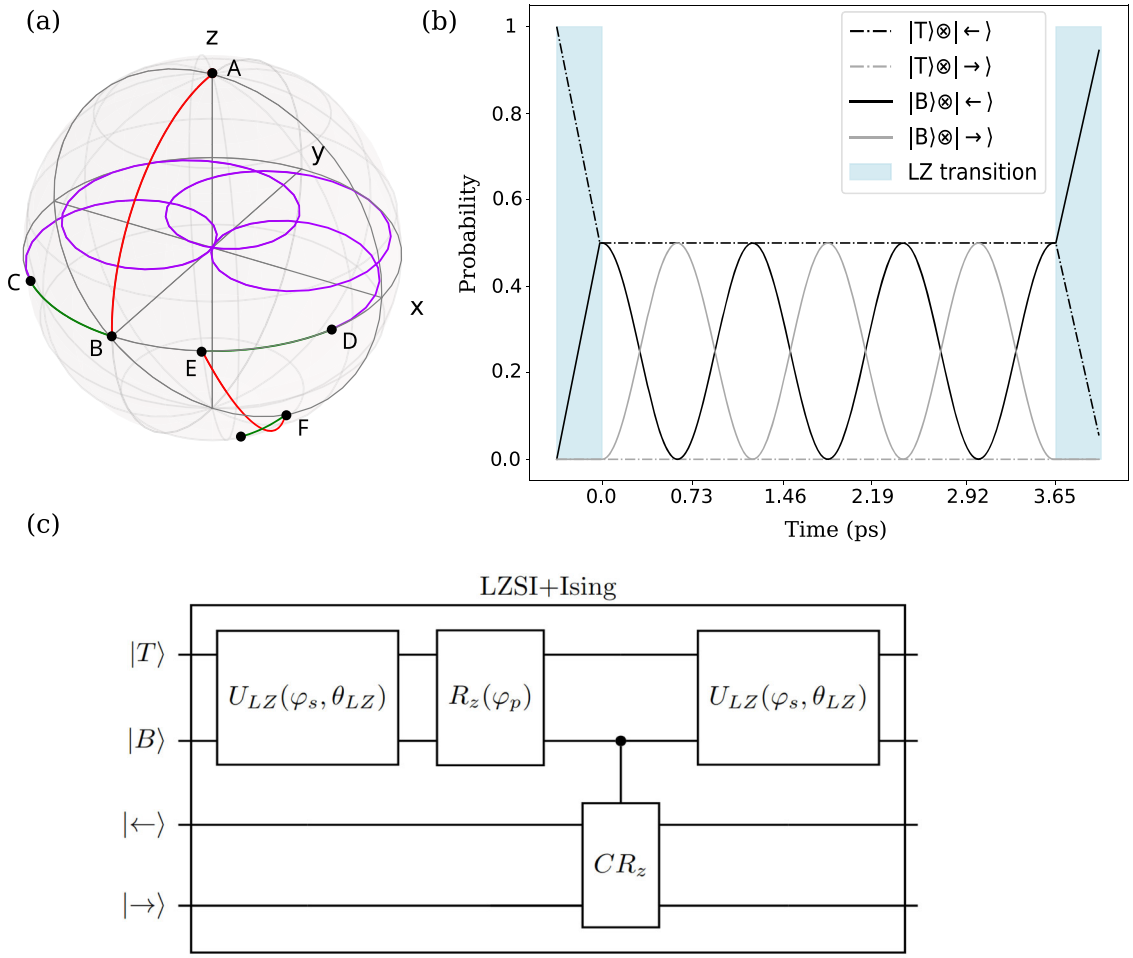

Fig. 8 | State evolution of the vdW charge qubit. a Bloch sphere representation of the layer DoF, i.e., partial trace of the spin-charge density matrix. **b** Evolution of state probabilities during the LZSI. The dotted-dashed and the solid black lines denote the $|T\rangle \otimes |\leftarrow\rangle$ and $|B\rangle \otimes |\leftarrow\rangle$ states, respectively. The dotted-dashed and solid grey lines denote the $|T\rangle \otimes |\rightarrow\rangle$ and $|B\rangle \otimes |\rightarrow\rangle$ states, respectively. The LZSI commences with a LZ transition (left blue shaded region) and ends with the second LZ transition (right blue shaded region). In between, the system experiences phase accumulation and spin rotations. In the proposed setup, we have $t_{\mathrm{LZSI}} \gg t_{\mathrm{LZ}}$ for the duration of LZ transitions, and therefore, the time axis during LZ transitions is enlarged for better visibility and does not have the same time scale as the phase accumulation. **c** Quantum circuit corresponding to the LZSI mechanism.

relationship between the final state probabilities at the end of LZSI and the duration of phase accumulation t_{LZSI}, as shown in Fig. 9 for a large range of values. The time evolution in Fig. 8 is obtained with $t_{\mathrm{LZSI}} \simeq 3.72$ ps, which can achieve a $R_x(\pi)$ rotation of the charge qubit without rotation on the spin qubit. We obtain the overlap between the final state and the target state: $|T\rangle \otimes |\leftarrow\rangle \mapsto |\psi\rangle$ with $|\langle\psi|(|B\rangle \otimes |\leftarrow\rangle)|^2 \simeq 0.995$.

The above results are obtained with the following effective Hamiltonian under a time-dependent inter-layer potential difference $V(t)$

$$H_{\mathrm{LZSI}}(t) = \frac{V(t)}{2}\sigma_z + T_{\mathrm{LZ}}(t)\sigma_x + H_{\mathrm{LZSI}|Ising}, \tag{9}$$

where $T_{\mathrm{LZ}}(t)$ denotes the physical inter-layer tunneling energy. Here, the Pauli matrices σ_x and σ_z act only on the charge DoF spanned by $\{|\mathrm{T}\rangle, |\mathrm{B}\rangle\}$. Both V and T_{LZ} are time-dependent due to the modulating electric field. The last term $H_{\mathrm{LZSI}|Ising}$ in the Hamiltonian captures the effect of Ising SOC. The spin interaction of the LZSI Hamiltonian reads

$$H_{\mathrm{LZSI}|Ising} = \lambda_I^{A2}\mathcal{P}_B s_z \mathcal{P}_B + \lambda_I^{A1}\mathcal{P}_T s_z \mathcal{P}_T, \tag{10}$$

where $\lambda_I^{A2/A1}$ are the Ising SOC parameters in the bottom/top layer (Table 1), respectively, and s_y is the Pauli spin matrix. Since $\lambda_I^{A2} \gg \lambda_I^{A1}$, the spin rotates only when the bottom layer is populated. The projection to top and bottom layer subspaces is denoted as $\mathcal{P}_T$ and $\mathcal{P}_B$, respectively.

To calibrate the effective inter-layer tunneling energy T_{LZ} in Eq. (9), the 2 × 2 LZSI Hamiltonian must be diagonalized for different potential values V, corresponding to the vertical electric fields used in the DFT calculations and reported in Table 1. The LZSI eigenenergies are then fitted to the DFT results. This gives the field-dependent value of the tunneling energy, for both spin-up and spin-down, with minimum value $T_{\mathrm{LZ}}^{*} = 0.73$ meV at the anti-crossing point. In this study, we approximate the pulse shape that implements LZSI with a rectangular function, i.e., $V(t) = V_0 + [\Theta(t) - \Theta(t - t_{\mathrm{LZSI}})]V\prime$, where $\Theta(t)$ is the unit step function. Further details about the LZSI and model parameters are provided in the SI.

Combined spin-charge manipulation. Due to the layer-selective SOC in the BLG-WSe_2 vdWh, the charge qubit state must be $|\mathrm{B}\rangle$ for the strong Ising SOC to drive fast spin rotation. Therefore, the charge qubit serves as a valve to switch on and off the spin rotation, i.e., to act as a CR_z gate. Based on this mechanism, by controlling the phase φ_p accumulated between the LZ transitions, one can implement a controlled NOT (CNOT) gate on the spin qubit using the charge qubit as the control unit. Since this protocol is based on the intrinsic SOC of the BLG-WSe_2 vdWh, it can be electrically driven without any external magnetic field. Combining the single-qubit rotation gates described in the previous subsections and the CNOT gate, we have all

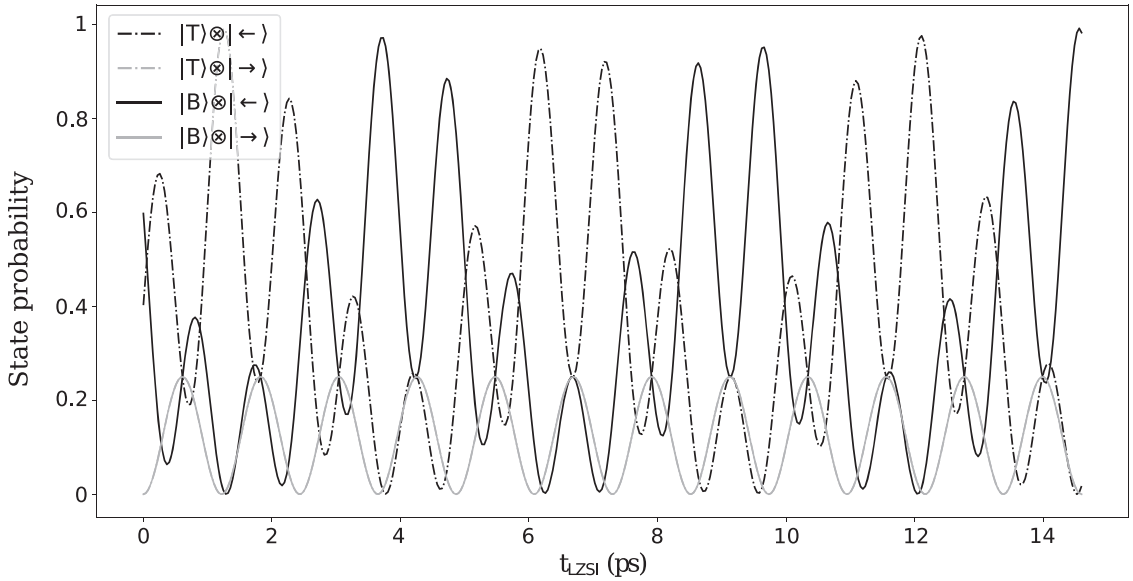

Fig. 9 | State probability for the four basis states of the two-qubit system for a long range of phase accumulation times t_{LZSI}. The dotted-dashed and the solid black lines denote the $|T\rangle \otimes |\leftarrow\rangle$ and $|B\rangle \otimes |\leftarrow\rangle$ states, respectively. The dotted-dashed and solid grey lines denote the $|T\rangle \otimes |\rightarrow\rangle$ and $|B\rangle \otimes |\rightarrow\rangle$ states, respectively. This is not a state evolution as in Fig. 8b, but rather represents a parameter sweep of t_{LZSI} for the final state probabilities after the LZSI sequence. In the plot, the probabilities for $|T\rangle \otimes |\rightarrow\rangle$ and $|B\rangle \otimes |\rightarrow\rangle$ are identical because they are initialized with zero population.

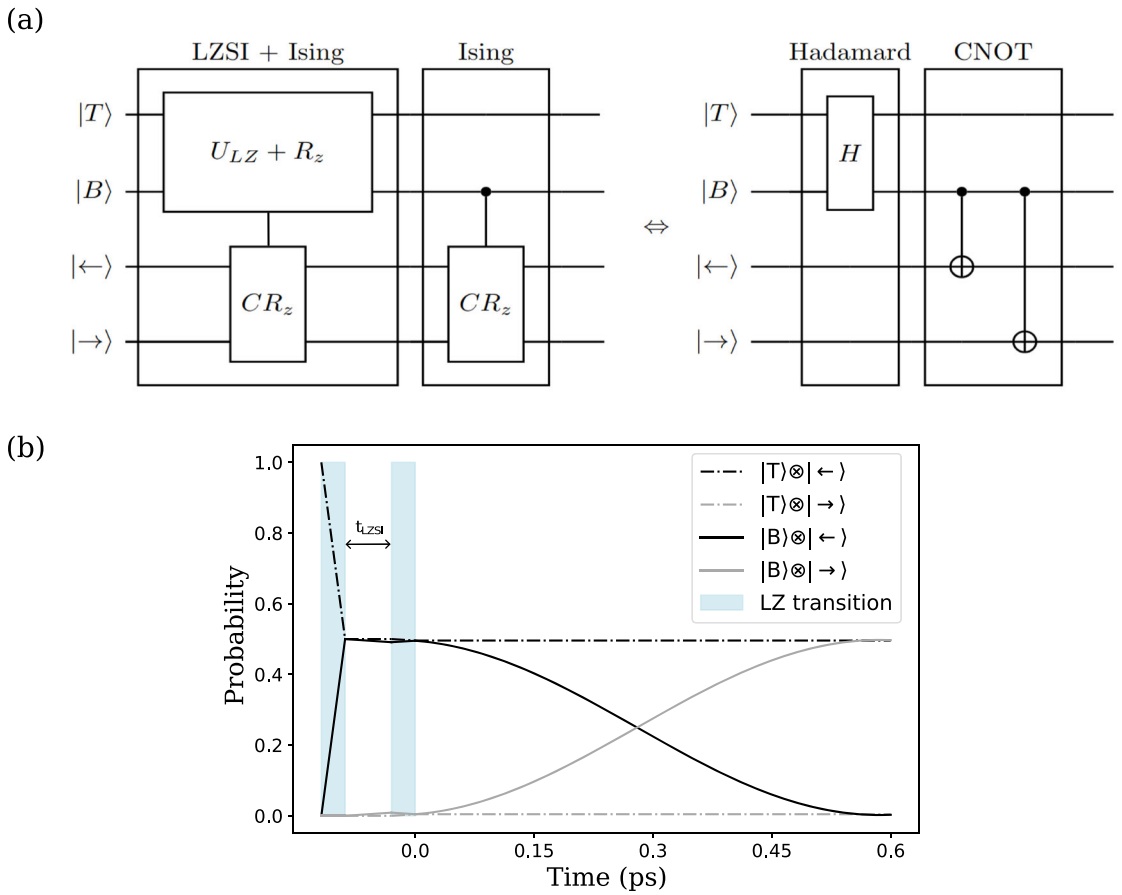

Fig. 10 | Entanglement of spin and charge qubits. a Performing a LZSI and a succeeding pure Ising rotation creates a maximally entangled state. The action of LZSI (U_{LZ} and R_z) and Ising (CR_z) on the two-qubit system (left part) is equivalent to the combination of a Hadamard (H) and CNOT gate (right part) for tunable evolution times. **b** Evolution of state probabilities corresponding to the circuits in (a). The dotted-dashed and the solid black lines denote the $|T\rangle \otimes |\leftarrow\rangle$ and $|B\rangle \otimes |\leftarrow\rangle$ states, respectively. The dotted-dashed and solid grey lines denote the $|T\rangle \otimes |\rightarrow\rangle$ and $|B\rangle \otimes |\rightarrow\rangle$ states, respectively. The LZ transitions act in the blue shaded region and are not to scale with the x-axis.

the necessary building blocks to implement basic quantum circuits based on a single QD in our BLG-WSe_2 system.

As an illustration, taking advantage of the LZSI operation, we can define a sequence to entangle the spin and charge qubits. This is depicted in Fig. 10a and b. The system is first initialized in the $|T\rangle \otimes |\leftarrow\rangle$ state, i.e., in the charge state $|T\rangle$ and spin state $|\leftarrow\rangle$. By applying an LZSI pulse, the electron is pushed into a charge superposition state $(|T\rangle + |B\rangle) \otimes |\leftarrow\rangle/\sqrt{2}$. After the LZSI pulse, the Ising SOC continues to rotate the spin in the bottom layer (see Fig. 10b), such that we finally obtain an entangled state $|\Psi\rangle = (|T\rangle \otimes |\leftarrow\rangle + |B\rangle \otimes |\rightarrow\rangle)/\sqrt{2}$. The result is a non-separable state of the bipartite Hilbert space $\{|B\rangle, |T\rangle\} \otimes \{|\leftarrow\rangle, |\rightarrow\rangle\}$ composed of the spin and charge states. The equivalent quantum circuit corresponding to this process and involving Hadamard and CNOT gates is shown in the right part of Fig. 10a. To measure the degree of entanglement of the final state $|\Psi\rangle$, we quantify the entanglement entropy, i.e., the von Neumann entropy of the reduced density matrix of the charge qubit subsystem. We compute an entanglement entropy $S_{\text{charge}} \simeq 0.693 \simeq \ln(2)$, which indicates the existence of large entanglement between the spin and charge DoFs.

Discussion

We discuss here the limitations of the proposed spin-charge BLG-WSe_2 qubits within an open quantum system, followed by real-world challenges in fabrication and implementation. In the end of this section, we compare metrics predicted by our model with those from the literature about promising qubit platforms.

The Hamiltonians for EDSR (Eq. (8)) and LZSI (Eq. (9)) describe the spin-charge qubit in a closed system, but since real quantum systems are open, their dynamics will be different. The most prominent effect of the environment on the state evolution of the spin-charge qubit is information leakage from the two-qubit subspace. As a consequence, for longer evolutions, the total occupation probability of states does not sum to one. This affects the fidelity of operations such as the entanglement sequence outlined in **Gate operation for the spin-charge qubit**. If the total probability of the state is not unity, the entanglement entropy is not maximal. However, a quantitative estimation of decoherence channels via simulations of open quantum systems is outside the scope of this study.

Practically, several challenges are associated with the fabrication of the vdW heterostructure to be used as a building block of robust qubits. First, graphene, WSe_2, and hexagonal boron nitride layers that encapsulate them are defective crystals. The presence of interface roughness and crystalline imperfections modifies the electronic structure[45]. Defects also perturb the local electrostatic potential. Both effects result in energy levels and charge densities deviating from the ab initio calculations of a perfect crystal structure. Due to the randomness distribution of defects, the energy level shifts may vary from device to device, thus requiring individual calibration to align them. Furthermore, crystalline imperfections can negatively impact qubit coherence by inducing additional nuclear spins, which decrease the coherence time and gate fidelity. In addition, heat dissipation can cause thermal excitations, leading to undesired spin relaxations. As a result, the thermal fluctuations limit the qubit coherence time and the gate fidelity. Such phenomena have been demonstrated by Camenzind et al.[46] with a hole spin qubit in a Silicon FinFET.

In addition to the fabrication of clean heterostructure, precise alignment during stacking of the graphene layers and the TMDC monolayer is also a crucial factor, as the relative twist angle can significantly increase the resulting SOC strength, as discussed in[47,48]. Despite these technical difficulties, the fabrication of BLG-TMDC heterostructures has been successfully achieved using polymer-based dry transfer and hot pick-up techniques[14,49–52]. Recently, the enhanced SOC in BLG has been experimentally confirmed and measured in a BLG-MoS_2 heterostructure[14].

The BLG-WSe_2 heterostructure is unique compared to other promising qubit platforms, since the SOC can be electrically controlled by the gate voltage over a large range of values. Such tunability is a major advantage over pure BLG, enabling the qubit to be dynamically tuned to operate with a long coherence time or fast operation speed. Furthermore, the BLG-WSe_2 heterostructure can also host a charge qubit, which has a very fast operation speed but is likely less resilient to the noise from the environment[53].

Since there have not yet been any experimental results on the BLG-WSe_2 heterostructure, we take the BLG platform as our reference for comparison with other qubit platforms. The BLG spin qubit has been proved in experiments to have a very long coherence time around 0.4 s. Recently, the coherence time has increased to 38 seconds with the exploitation of valley Kramer states[54]. Compared to silicon, which is the leading semiconductor platform for spin qubit, the BLG is advantageous with respect to both coherence time and operation speed[6]. The superconducting qubits have an operation speed similar to that of the BLG qubit. However, they have a coherence time between 10 and 100 μs[2–4], which is shorter than the BLG qubit, and they require a complicated setup, including high-quality microwave resonators and cryogenic instruments. Lastly, to conclude the comparison with existing platforms, the topological qubit (as proposed in ref. 55) should be more robust than the other platforms because of the topological protection against noise based on its nonlocal encoding. However, a relatively slow gate time and a more complicated setup are expected.

In this work, we investigated a BLG-WSe_2 vdWh system that supports both charge and spin qubits by leveraging the proximity effect induced by WSe_2 and the layer polarization of BLG. We extracted the SOC coefficients of the graphene layers and $k \cdot p$ model parameters to represent their band dispersion from ab initio calculations. Based on this calibrated model, we confirmed the large enhancement of SOC in the graphene layer adjacent to WSe_2, an effect that was originally proposed by Gmitra et al.[19]. Through self-consistent Schrödinger-Poisson calculations, the formation of electrically confined electron and hole quantum dots in the BLG was studied. The gate voltage dependence of the dot area, shape, and energy levels was computed before discussing layer mixing and its relationship to the confinement potential. It was then demonstrated that the SOC of the electron- and hole-quantum dot can be electrically turned on and off by applying a vertical electric field, allowing for the creation of fully electrically controlled spin qubits. Since electron and hole quantum dots display symmetric properties in BLG-WSe_2 vdWh, the design of qubit arrays exploiting both types of qubits is greatly simplified. We also constructed a simplified model Hamiltonian describing the time evolution of the spin and charge states. Our simulations revealed that the proposed qubit operations have a time scale in the order of picoseconds. Finally, we suggested the possibility of performing EDSR operations on the graphene layer adjacent to WSe_2 through external electric fields and to combine them with LZSI operations to entangle the spin and charge degrees of freedom of an electron or hole in a BLG quantum dot. Both operations only require electric fields generated by the top and bottom gates.

This work highlights the potential of the proposed BLG-WSe_2 vdWh architecture as a spin-charge qubit and building block of future quantum information processors. Investigations of multiple BLG quantum dots are now needed to better understand inter-dot Coulomb interaction and tunneling energies. If promising, these results, combined with the relatively simple gate setup of the BLG-WSe_2 system, could open the door for dense spin-qubit 2D arrays with long-distance coupling between individual devices[56]. As a future study, it could be envisioned that the valley degree of freedom of BLG-WSe_2 is further leveraged by applying small magnetic fields.

Methods

The DFT package VASP was employed to perform the ab initio calculations of the bilayer graphene and WSe_2 heterostructure using the generalized gradient approximation (GGA) of Perdew, Burke, and Ernzerhof (PBE)[57]. A super-cell was constructed with 4×4 bilayer graphene and 3×3 WSe_2, as depicted in Fig. 2. A Γ-centered Monkhorst-Pack k-point grid of dimension $3 \times 3 \times 1$ and a plane-wave cutoff energy of 850 eV were used. The DFT-D3 method of Grimme[58] accounts for the van der Waals interactions. For the forces acting on each ion, a convergence criterion smaller than 10^{-4} eV/Å was applied, while the total energy difference between two subsequent iterations was smaller than 10^{-6} eV. A large vacuum of 34 Å was placed along the stacking direction to avoid spurious interactions from the periodic

replica in the out-of-plane direction. To include the important spin-orbit coupling and electric field effects, the noncollinear calculations and dipole correction were accounted in the electronic ground state and band structure calculations.

k · p model

The Hamiltonian used to model the pristine bilayer graphene as well as our heterostructure, is inspired by[38]. As schematically shown in Fig. 2, it only takes into account the bilayer graphene states originating from the A and B atoms in layers 1 or 2.

The Hamiltonian $\mathcal{H} = \mathcal{H}_{\rm orb} + \mathcal{H}_{\rm soc} + E_D$ includes a tight-binding and spin-orbit coupling part, as specified below. As the WSe_2 states lie outside the energy region of interest, they are neglected. An additional Dirac energy offset E_D is introduced to improve the fitting. The total Hamiltonian is given in the basis $\{|C_{A1},\uparrow\rangle, |C_{A1},\downarrow\rangle, |C_{B1},\uparrow\rangle, |C_{B1},\downarrow\rangle, |C_{A2},\uparrow\rangle, |C_{A2},\downarrow\rangle, |C_{B2},\uparrow\rangle, |C_{B2},\downarrow\rangle\}$.

$$\mathcal{H}_{\rm orb} = \begin{pmatrix} \Delta + V & \gamma_0 f(k) & \gamma_4 f^*(k) & \gamma_1 \\ \gamma_0 f^*(k) & V & \gamma_3 f(k) & \gamma_4 f^*(k) \\ \gamma_4 f(k) & \gamma_3 f^*(k) & -V & \gamma_0 f(k) \\ \gamma_1 & \gamma_4 f(k) & \gamma_0 f^*(k) & \Delta - V \end{pmatrix} \otimes s_0. \tag{11}$$

$$\mathcal{H}_{\rm soc} = \begin{pmatrix} \tau\lambda_I^{A_1} s_z & \mathrm{i}(\lambda_0 + 2\lambda_R)s_-^\tau & 0 & 0 \\ -\mathrm{i}(\lambda_0 + 2\lambda_R)s_+^\tau & -\tau\lambda_I^{B_1} s_z & 0 & 0 \\ 0 & 0 & \tau\lambda_I^{A_2} s_z & -\mathrm{i}(\lambda_0 - 2\lambda_R)s_-^\tau \\ 0 & 0 & \mathrm{i}(\lambda_0 - 2\lambda_R)s_+^\tau & -\tau\lambda_I^{B_2} s_z \end{pmatrix}. \tag{12}$$

The γ_0 and γ_1 parameters denote the nearest-neighbor intra- and interlayer hopping, whereas γ_3 and γ_4 refer to the indirect hopping between the layers. The potential felt by each layer is given by $\pm V$. The staggered potential Δ is an additional energy shift used to handle the asymmetries of the corresponding bonding and antibonding states in the dimer orbitals A_1, B_2 due to γ_1[38]. To shorten the notation the following operators are defined $s_\pm^\tau = \frac{1}{2}(s_x \pm \mathrm{i}\tau s_y)$, where the operators $s_i = \frac{1}{2}\sigma_i$ denote the spin matrices. We use the same linearized version of the nearest-neighbor structural function $f(k) = -\frac{\sqrt{3}a}{2}(\tau k_x - \mathrm{i}k_y)$ as in ref. 59. The graphene lattice constant is labeled as a, and the wave vectors k_x, k_y are measured from K (or K') for a valley index $\tau = 1$ (or $\tau = -1$), respectively.

The spin-orbit coupling coefficients of orbitals originating from atoms A, B in layer j on the diagonal are given by $\lambda_I^{A_j}$ and $\lambda_I^{B_j}$, respectively. As the induced spin-orbit coupling in the bilayer graphene layers is of the valley-Zeeman type, with opposite signs on the atoms of the sublattice, we set $\lambda_I^{A_j} = -\lambda_I^{B_j}$. The λ_0 denotes the local breaking of space inversion due to the presence of the other layer in BLG, λ_R indicates the global breaking of space inversion symmetry due to the heterostructure and the electric field[59].

Schrödinger-Poisson solver

Our Schrödinger solver relies on the 8 × 8 Hamiltonian of Eq. (1), which is discretized on a finite difference grid. To transform $\mathcal{H} = \mathcal{H}_{\rm orb} + \mathcal{H}_{\rm soc}$ from the k-space to the real-space, we follow the prescription $k_x \to i\partial_x$ and $k_y \to i\partial_y$. To solve the well-known Fermion doubling problem at $k = \pm\pi$, we add a tiny quadratic term $(k_x^2 + k_y^2)$ to the discretized Hamiltonian according to Susskind's work[60]. A discretization step of 1 nm is used along x and y directions, while 0.4 nm in z direction. By using a smaller discretization step of 0.5 nm along x and y, the QD energy levels differ by around 30μeV, proving the convergence of the grid. The details of the tight-binding Hamiltonian $\mathcal{H}_{\rm orb}$ and the spin-orbit Hamiltonian $\mathcal{H}_{\rm soc}$ are specified in **k·p model**. The fitting parameters $\gamma_i, \lambda_I^{A_i}, V$, and Δ are taken from the $E = 0.25$ V/nm entries of Table 1.

The Schrödinger solver takes as input the electrostatic potential of each graphene layer obtained from a 3-D Poisson solver. This potential is first super-sampled from a coarser grid (4 nm × 4 nm discretization step) to a refined grid (1 nm × 1 nm discretization step) by spline interpolation. After adding the electrostatic potential to the diagonal elements of the discretized 8-band k · p Hamiltonian matrix, the Schrödinger solver diagonalizes it using Scipy and ARPACK[61,62], which produces the eigenstates and eigenenergies of the system of interest. Only the lowest/highest energies above/below the Fermi level are retained. Finally, the charge density $\rho^{\rm new}$ is computed as the norm square of the wave function. The difference between $\rho^{\rm new}$ and $\rho^{\rm old}$ from the previous iteration defines the error of the Schrödinger-Poisson self-consistent loop:

$$\text{Error} = \sum_{ij} \frac{|\rho_{ij}^{\rm new} - \rho_{ij}^{\rm old}|}{\rho_{ij}^{\rm old}} \tag{13}$$

The 3D Poisson solver takes the charge density in the two graphene layers of BLG obtained from the Schrödinger solver as input. Starting with an automatic cycle that adjusts the gate voltages to meet the requirement of charge confinement potential. The Poisson solver determines the new potential in the 3-D grid of 4 nm × 4 nm × 0.4 nm discretization step, extracts out the potential inside the Schrödinger region consisting of the two graphene layers, and passes it to the Schrödinger solver. This Schrödinger-Poisson iterative process stops when the self-consistent relative error ≤0.001 is reached.

Data availability

Data sets generated during the current study are available from the corresponding author on reasonable request. The dataset on DFT band structure and quantum dot energies is available at https://doi.org/10.3929/ethz-b-000731746.

Received: 25 February 2025; Accepted: 12 May 2025;
Published online: 11 June 2025

References

1. Kjaergaard, M. et al. Superconducting qubits: current state of play. *Annu. Rev. Condens. Matter Phys.* **11**, 369–395 (2020).
2. Siddiqi, I. Engineering high-coherence superconducting qubits. *Nat. Rev. Mater.* **6**, 875–891 (2021).
3. Burnett, J. J. et al. Decoherence benchmarking of superconducting qubits. *npj Quantum Inf.* **5**, 54 (2019).
4. Lisenfeld, J., Bilmes, A. & Ustinov, A. V. Enhancing the coherence of superconducting quantum bits with electric fields. *npj Quantum Inf.* **9**, 8 (2023).
5. Hanson, R., Kouwenhoven, L. P., Petta, J. R., Tarucha, S. & Vandersypen, L. M. K. Spins in few-electron quantum dots. *Rev. Mod. Phys.* **79**, 1217–1265 (2007).
6. Zwanenburg, F. A. et al. Silicon quantum electronics. *Rev. Mod. Phys.* **85**, 961–1019 (2013).
7. Noiri, A. et al. Fast universal quantum gate above the fault-tolerance threshold in silicon. *Nature* **601**, 338–342 (2022).
8. Mills, A. et al. High-fidelity state preparation, quantum control, and readout of an isotopically enriched silicon spin qubit. *Phys. Rev. Appl.* **18**, 064028 (2022).
9. Scappucci, G. et al. The germanium quantum information route. *Nat. Rev. Mater.* **6**, 926–943 (2020).
10. Hendrickx, N. W., Franke, D. P., Sammak, A., Scappucci, G. & Veldhorst, M. Fast two-qubit logic with holes in germanium. *Nature* **577**, 487–491 (2020).
11. Hendrickx, N. W. et al. Sweet-spot operation of a germanium hole spin qubit with highly anisotropic noise sensitivity. *Nat. Mater.* **23**, 920–927 (2024).
12. Han, W., Kawakami, R. K., Gmitra, M. & Fabian, J. Graphene spintronics. *Nat. Nanotechnol.* **9**, 794–807 (2014).
13. Eich, M. et al. Spin and valley states in gate-defined bilayer graphene quantum dots. *Phys. Rev. X* **8**, 031023 (2018).

14. Masseroni, M. et al. Spin-orbit proximity in MoS2/bilayer graphene heterostructures. *Nat. Commun.* **15**, 9251 (2024).
15. Garreis, R. et al. Long-lived valley states in bilayer graphene quantum dots. *Nat. Phys.* **20**, 428–434 (2024).
16. Gächter, L. M. et al. Single-shot spin readout in graphene quantum dots. *PRX Quantum* **3**, 020343 (2022).
17. Castro, E. V. et al. Biased bilayer graphene: Semiconductor with a gap tunable by the electric field effect. *Phys. Rev. Lett.* **99**, 216802 (2007).
18. Banszerus, L. et al. Single-Electron Double Quantum Dots in Bilayer Graphene. *Nano Lett.* **20**, 2005–2011 (2020).
19. Gmitra, M. & Fabian, J. Proximity effects in bilayer graphene on monolayer WSe2: Field-effect spin valley locking, spin-orbit valve, and spin transistor. *Phys. Rev. Lett.* **119**, 146401 (2017).
20. Wang, Z. et al. Strong interface-induced spin–orbit interaction in graphene on WS2. *Nat. Commun.* **6**, 8339 (2015).
21. Golovach, V. N., Borhani, M. & Loss, D. Electric-dipole-induced spin resonance in quantum dots. *Phys. Rev. B* **74**, 165319 (2006).
22. Khoo, J. Y., Morpurgo, A. F. & Levitov, L. On-demand spin–orbit interaction from which-layer tunability in bilayer graphene. *Nano Lett.* **17**, 7003–7008 (2017).
23. Kim, D. et al. Microwave-driven coherent operation of a semiconductor quantum dot charge qubit. *Nat. Nanotechnol.* **10**, 243–247 (2015).
24. Ota, T., Hitachi, K. & Muraki, K. Landau-zener-stückelberg interference in coherent charge oscillations of a one-electron double quantum dot. *Sci. Rep.* **8**, 5491 (2018).
25. Hayashi, T., Fujisawa, T., Cheong, H. D., Jeong, Y. H. & Hirayama, Y. Coherent manipulation of electronic states in a double quantum dot. *Phys. Rev. Lett.* **91**, 226804 (2003).
26. Petersson, K. D., Petta, J. R., Lu, H. & Gossard, A. C. Quantum coherence in a one-electron semiconductor charge qubit. *Phys. Rev. Lett.* **105**, 246804 (2010).
27. Shinkai, G., Hayashi, T., Ota, T. & Fujisawa, T. Correlated coherent oscillations in coupled semiconductor charge qubits. *Phys. Rev. Lett.* **103**, 056802 (2009).
28. Shevchenko, S., Ashhab, S. & Nori, F. Landau–zener–stückelberg interferometry. *Phys. Rep.* **492**, 1–30 (2010).
29. Cao, G. et al. Ultrafast universal quantum control of a quantum-dot charge qubit using landau–zener–stückelberg interference. *Nat. Commun.* **4**, 1401 (2013).
30. Maurand, R. et al. A cmos silicon spin qubit. *Nat. Commun.* **7**, 13575 (2016).
31. Gao, W.-B. et al. Experimental demonstration of a hyper-entangled ten-qubit schrödinger cat state. *Nat. Phys.* **6**, 331–335 (2010).
32. Burkard, G., Ladd, T. D., Pan, A., Nichol, J. M. & Petta, J. R. Semiconductor spin qubits. *Rev. Mod. Phys.* **95**, 025003 (2023).
33. Kwiat, P. G. Hyper-entangled states. *J. Mod. Opt.* **44**, 2173–2184 (1997).
34. Barreiro, J. T., Langford, N. K., Peters, N. A. & Kwiat, P. G. Generation of hyperentangled photon pairs. *Phys. Rev. Lett.* **95**, 260501 (2005).
35. Fülöp, B. et al. Boosting proximity spin–orbit coupling in graphene/WSe2 heterostructures via hydrostatic pressure. *npj 2D Mater. Appl.* **5**, 82 (2021).
36. Tiwari, P. et al. Experimental observation of spin-split energy dispersion in high-mobility single-layer graphene/WSe2 heterostructures. *npj 2D Mater. Appl.* **6**, 68 (2022).
37. Kresse, G. & Furthmüller, J. Efficient iterative schemes for ab initio total-energy calculations using a plane-wave basis set. *Phys. Rev. B* **54**, 11169–11186 (1996).
38. Konschuh, S., Gmitra, M., Kochan, D. & Fabian, J. Theory of spin-orbit coupling in bilayer graphene. *Phys. Rev. B* **85**, 115423 (2012).
39. Bosco, S., Benito, M., Adelsberger, C. & Loss, D. Squeezed hole spin qubits in ge quantum dots with ultrafast gates at low power. *Phys. Rev. B* **104**, 115425 (2021).
40. Lucatto, B., Koda, D. S., Bechstedt, F., Marques, M. & Teles, L. K. Charge qubit in van der Waals heterostructures. *Phys. Rev. B* **100**, 121406 (2019).
41. Cao, J., Gandus, G., Agarwal, T., Luisier, M. & Lee, Y. Dynamics of van der Waals charge qubit in two-dimensional bilayer materials: Ab initio quantum transport and qubit measurement. *Phys. Rev. Res.* **4**, 043073 (2022).
42. McCann, E. & Koshino, M. The electronic properties of bilayer graphene. *Rep. Prog. Phys.* **76**, 056503 (2013).
43. Zou, K., Hong, X. & Zhu, J. Effective mass of electrons and holes in bilayer graphene: Electron-hole asymmetry and electron-electron interaction. *Phys. Rev. B* **84**, 085408 (2011).
44. Aleksandrowicz, G. et al. Qiskit: An open-source framework for quantum computing https://doi.org/10.5281/zenodo.2562111 (2019).
45. Rhodes, D., Chae, S. H., Ribeiro-Palau, R. & Hone, J. Disorder in van der Waals heterostructures of 2d materials. *Nat. Mater.* **18**, 541–549 (2019).
46. Camenzind, L. C. et al. A hole spin qubit in a fin field-effect transistor above 4 kelvin. *Nat. Electron.* **5**, 178–183 (2022).
47. Li, Y. & Koshino, M. Twist-angle dependence of the proximity spin-orbit coupling in graphene on transition-metal dichalcogenides. *Phys. Rev. B* **99**, 075438 (2019).
48. David, A., Rakyta, P., Kormányos, A. & Burkard, G. Induced spin-orbit coupling in twisted graphene–transition metal dichalcogenide heterobilayers: Twistronics meets spintronics. *Phys. Rev. B* **100**, 085412 (2019).
49. Island, J. O. et al. Spin–orbit-driven band inversion in bilayer graphene by the van der Waals proximity effect. *Nature* **571**, 85–89 (2019).
50. Yang, B. et al. Tunable spin–orbit coupling and symmetry-protected edge states in graphene/ws 2. *2D Mater.* **3**, 031012 (2016).
51. Amann, J. et al. Counterintuitive gate dependence of weak antilocalization in bilayer graphene/WSe2 heterostructures. *Phys. Rev. B* **105**, 115425 (2022).
52. Pizzocchero, F. et al. The hot pick-up technique for batch assembly of van der Waals heterostructures. *Nat. Commun.* **7**, 11894 (2016).
53. Hecker, K. et al. Coherent charge oscillations in a bilayer graphene double quantum dot. *Nat. Commun.* **14**, 7911 (2023).
54. Denisov, A. O. et al. Spin–valley protected Kramers pair in bilayer graphene. *Nat. Nanotechnol.* https://doi.org/10.1038/s41565-025-01858-8 (2025).
55. Aasen, D. et al. Roadmap to fault tolerant quantum computation using topological qubit arrays https://arxiv.org/abs/2502.12252 (2025).
56. Trauzettel, B., Bulaev, D. V., Loss, D. & Burkard, G. Spin qubits in graphene quantum dots. *Nat. Phys.* **3**, 192–196 (2007).
57. Perdew, J. P., Burke, K. & Ernzerhof, M. Generalized gradient approximation made simple. *Phys. Rev. Lett.* **77**, 3865–3868 (1996).
58. Grimme, S., Antony, J., Ehrlich, S. & Krieg, H. A consistent and accurate ab initio parametrization of density functional dispersion correction (DFT-D) for the 94 elements H-Pu. *J. Chem. Phys.* **132**, 154104 (2010).
59. Zollner, K., Gmitra, M. & Fabian, J. Swapping exchange and spin-orbit coupling in 2d van der Waals heterostructures. *Phys. Rev. Lett.* **125**, 196402 (2020).
60. Susskind, L. Lattice fermions. *Phys. Rev. D.* **16**, 3031–3039 (1977).
61. Virtanen, P. et al. SciPy 1.0: Fundamental algorithms for scientific computing in Python. *Nat. Methods* **17**, 261–272 (2020).
62. Lehoucq, R. B., Sorensen, D. C. & Yang, C. *ARPACK Users' Guide* (Society for Industrial and Applied Mathematics, 1998). https://doi.org/10.1137/1.9780898719628.

Acknowledgements

This work was supported by the NCCR SPIN (Grant number 180604) and the NCCR MARVEL (Grant number 205602) of the Swiss National Science

Foundation (SNSF). Computational resources were provided by the Swiss National Supercomputing Center (CSCS) under project No. s1119 and lp16.

Author contributions

J.C. and M.L. conceived the project. H.G., P.K., M.D., and J.C. carried out the DFT calculations. H.G. and F.M. prepared Fig 1. P.K. implemented the fitting of k.p model and prepared figs 2 and 3. H.G. and J.C. implemented the Schrödinger-Poisson solver. H.G., F.M., and I.B. carried out Schrödinger-Poisson simulations. H.G. prepared figs 4 and 5. O.S. implemented the time-dependent simulations and prepared figs 6-10. All authors discussed the results, wrote the main manuscript text, and reviewed the manuscript.

Competing interests

The authors declare no competing interests.

Additional information

Supplementary information The online version contains supplementary material available at https://doi.org/10.1038/s41699-025-00568-y.

Correspondence and requests for materials should be addressed to Mathieu Luisier or Jiang Cao.